

Extended X-ray Jets in Radio-loud Quasars: A Morphological Study

A Thesis Submitted by

Suresh Parekh

21021056

In partial fulfillment of the requirements of the degree of

Master of Science in Physics

Under The Supervision of

Dr. Vaidehi S. Paliya

Inter-University Centre for Astronomy and Astrophysics
Ganeshkhind, Pune 411 007, India

to

Department of Physics
Savitribai Phule Pune University
Pune, India



May, 2023

Department of Physics
Savitribai Phule Pune University

Project Certificate : PHY-C 400

1. Name of the Student:- Suresh Ambrish Parekh
2. Permanent Address:- RH-1, Green Park Society, Grid Road Kabilpore, Navsari, Gujarat - 396445
3. Permanent Registration No.:- 21021056
4. Name of the Teacher Guide:- Dr. Vaidehi Paliya (IUCAA)
5. Period of the Project:- August, 2022 to May, 2023
6. Title of the Project:- Extended X-ray Jets in Radio-loud Quasars: A Morphological Study
7. The Project work was carried out the candidate ALONE/~~JOINTLY~~ with
~~Mr./Miss.~~
8. The Project was continuation of pervious M.Sc, project ~~of Mr.~~
And/or is the part of research project entitled _____
9. **Theoretical:-** **Weightages**
 - a) Literature review %
 - b) Theoretical Calculation %
Based only on available
literature
 - c) New Theory and calculations %
10. **Experimental:-** **Weightages**
 - a) Equipments development %
 - b) Repeat work online of that
available in literature
 - c) New work %

Signature of Student

I certify that the student is regular student of the Department of Physics and has carried out the project, during period.

Signature of Teacher
Date:-

Head, Department of Physics
Savitribai Phule Pune University

Department of Physics
Savitribai Phule Pune University

Project Certificate : PHY-C400

This is to certify that the content of the project report or any part of it is not copied verbatim from any sources, such as journals, books, magazines, reports, Ph.D. / M.Phil. thesis, websites etc. In cases, where certain sentences / paragraphs / figures etc. are copied verbatim, I have mentioned these within “quotes” and with due reference to the source(s) . I would also like to certify that full reference is given whenever research work of other researchers is mentioned in the project report.

Name of the student: Suresh Ambrish Parekh

Signature of the student: _____

PRN of the student: 2201003257 / 21021056

Acknowledgement

I want to take this opportunity to express my heartfelt gratitude towards the individuals who have contributed to the successful completion of my master's thesis.

First and foremost, I would like to thank my thesis advisor, Dr. Vaidehi Paliya, for his unwavering support, guidance, and mentorship throughout the process. His insights, constructive feedback, and timely advice were instrumental in shaping my research project and enabling me to achieve my academic goals.

I also extend my appreciation to the faculty members of the Department of Physics, Savitribai Phule Pune University for their valuable feedback and constructive criticism have been pivotal in strengthening my research work and making it more impactful.

Furthermore, I would like to thank my friends and family members for their constant support, encouragement, and motivation during my academic journey. Their support and love have kept me going even during the most challenging times of my research work.

I would also like to acknowledge and thank the Chandra Helpdesk for providing me constant support throughout my project. Their contribution to my research has been significant, and I am deeply grateful for their cooperation and support.

In conclusion, I express my sincere appreciation towards all those who have contributed to my research project in various ways. Their support, guidance, and encouragement have been indispensable, and I am grateful for their contributions towards completing my master's thesis.

Suresh Parekh

Contents

1	Introduction	1
1.1	Active Galactic Nuclei	2
1.2	Components of AGN	3
1.3	Classification of AGN	4
1.3.1	Radio-loud AGN	4
1.3.2	Radio-quiet AGN	5
1.4	AGN Unification	6
2	Review of Related Literature	8
2.1	Quasars	8
2.2	Classification of Quasars	8
2.3	Relativistic Jets	9
2.4	Motivation of the Work	10
3	Data Analysis and Methodology	12
3.1	<i>Chandra</i> X-Ray Observatory	12
3.2	<i>Chandra</i> Data	13
3.3	<i>Chandra</i> Interactive Analysis of Observations (CIAO)	14
3.4	Downloading and Calibrating Data	14
3.5	Creating exposure Corrected Image	15
3.6	Generating PSF	15
3.6.1	Generating Spectrum File:	16
3.6.2	Retrieving ChaRT Rays	16
3.6.3	Using MARX to Create an Event file from ChaRT Rays	17
3.7	LIRA: Low-counts Image Reconstruction and Analysis	19
3.8	Quantifying Evidence for Extended Jet Emission Using LIRA	20
3.9	Using Python and <i>pylira</i>	21
4	Results	23
5	Conclusion	26

List of Figures

1.1	Hubble Fork Diagram	2
1.2	Schematic of AGN Components	4
1.3	Schematic of AGN Unification scheme	7
2.1	AGN with a jet	10
2.2	Reconstructed Image of source 0730+257 using LIRA	11
3.1	<i>Chandra</i> Observatory	13
3.2	(a) Raw 0.5-7 keV image of quasar PKS 065-08, (b) exposure corrected and binned to 0.492 arcsec image of quasar PKS 065-08	14
3.3	Energy Spectrum of PKS 065-08	17
3.4	a) PSF of PKS 065-08 generated by marx , (b) background image of PKS 065-08, (c) Exposure image of PKS 065-08, (d) simulated baseline model for PKS 065-08 using fake function.	22
4.1	Test plot obtained by running the pipeline for the demo dataset	24
4.2	LIRA output for PKS 065-08	25

Chapter 1

Introduction

Galaxies are the gravitationally bound system of stars, dust and dark matter, and they form the individual large-scale structure in our Universe. The Sun is a star in our galaxy called Milky Way. The mass of the galaxies can range from $10^6 M_{\odot}$ (dwarf galaxies) to $10^{12} M_{\odot}$ (giant ellipticals), where M_{\odot} is the mass of the Sun. Morphologically, Galaxies can be classified based on Hubble's Fork diagram into three broad classes, namely the Elliptical (E), Spirals (S) and Spirals with prominent bars (Barred Spirals (Sb)) as shown in Figure 1.1.

Elliptical are older galaxies with little or no active star formation going on in them. Depending upon the ellipticity, they are classified on the fork diagram as E0 to E7. The Spiral Galaxies are generally associated with young stars and show a characteristic fine structure in the morphology—the presence of a compact core or Nucleus and the surrounding Spiral arms. Depending upon the spiral arms' density and compactness, Spirals are classified into S_a to S_c . Barred spirals differ from normal spirals because of a 'bar-like' structure near the disk. Depending on the bar's prominence, this galaxy-class is classified into Sb_a to Sb_c .

The individual stars contribute to the luminosity of these galaxies. Their radiation typically follows the blackbody spectra, but a significant fraction of non-thermal emission can be seen in the radio window due to synchrotron emission from supernova remnants and the interstellar medium. A small fraction of galaxies exhibit very energetic phenomena besides their normal emission. These galaxies are of interest to this work, and we will discuss them in more detail.

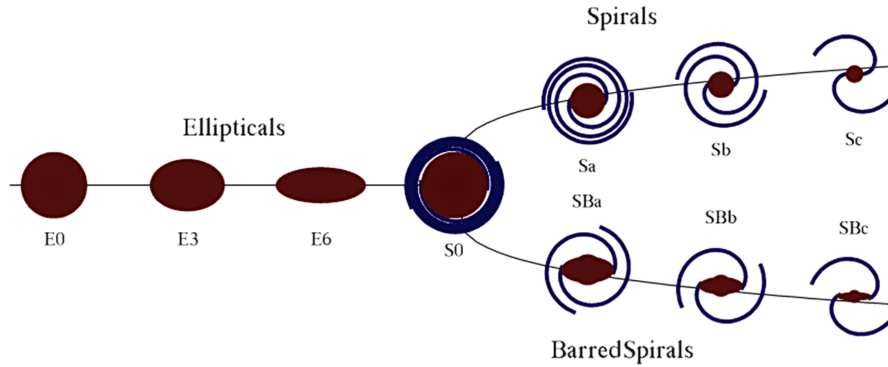


Figure 1.1: Hubble Fork Diagram giving morphological classification of galaxies

1.1 Active Galactic Nuclei

Active Galactic Nuclei (AGN) are centres of galaxies that are “active”. The accretion of matter powers them onto a supermassive black hole (SMBH), and emits large amounts of energy across the electromagnetic spectrum. AGN can be observed across vast distances and provide astronomers with valuable information about the formation and evolution of galaxies. AGNs are classified based on their observed properties, such as spectral lines, radio emission, and variability. The most common classification scheme is based on the presence or absence of broad emission lines in their spectra. AGN with broad emission lines is called Type 1 AGN, while those without are called Type 2 AGN. Other types of AGN include radio-loud and radio-quiet AGN and low-ionization nuclear emission-line regions (LINERs).

AGNs are essential for understanding galaxies’ growth and evolution and for testing theories of black hole accretion and jet formation. AGN-hosting galaxies are referred as active galaxies. AGN is usually unresolved, with the exception of the radio frequency, where there is occasionally proof of collimated outflows moving at relativistic velocities. AGN’s power output fluctuates often over timescales of years and occasionally over timescales of days, hours, or even minutes. According to the current theory, active galaxies have a supermassive black hole at their centre that takes in matter. The falling mass then releases a portion of its gravitational potential energy as

radiation. Some of these objects seemed roughly point-like or quasi-stellar in photographs, and as a result, they were also termed as quasi-stellar radio sources, or Quasars.

1.2 Components of AGN

AGNs are made up mainly of the following six components (see figure 1.2):

1. **Supermassive Black Hole:** SMBH has mass $\approx 10^6 - 10^{10} M_{\odot}$. It has also been proposed that every galaxy has a central SMBH. We also have considerable observational evidence, like imaging with the Event Horizon Telescope and Stellar motion at the center of the Milky Way.
2. **Accretion Disk:** Infalling gas forms the accretion disk in the galactic core. The assumption is that the disc viscosity is adequate to transfer outward angular momentum to the gas, allowing it to spiral into the centre. The temperature of the disk rises due to viscosity, and it varies depending on the distance from the centre. As a result, it will exhibit a multi-temperature blackbody spectrum. It is referred to be an AGN's "Central Engine" when combined with the BH. The accretion disk is typically a few light days in size.
3. **Broad-Line Region:** Gas clouds surround the Central Engine. It absorbs UV or X-ray energy photons from the engine and emits distinct lines as a result. When we examine it, the rotational motion of the cloud broadens it. Broad Line Region (BLR) clouds travel at a high speed of $\sim 3000 - 10000$ km/s around the centre engine. BLR Cloud has an average distance of $10 - 1000$ light days and a gas density of $10^9/cm^3$. The average BLR cloud mass is less than $10 M_{\odot}$.
4. **Narrow Line Region:** The clouds rotating further away are called Narrow Line Regions (NLRs). The typical distance of NLR cloud is $\sim 100 - 1000$ light-years with a low-velocity of $\sim 200 - 900$ km/s. They have a gas density of $\sim 10^3 - 10^5/cm^3$.
5. **Torus:** A Donut-shaped torus of gas and dust surrounds the core engine. The absorbed ultraviolet and X-ray energy is converted into infrared radiation by this dust cloud. Torus is typically a few hundred light years in size.
6. **Relativistic Jets:** Some AGN have highly collimated and relativistic outflows of plasma blobs in space perpendicular to the accretion disk on

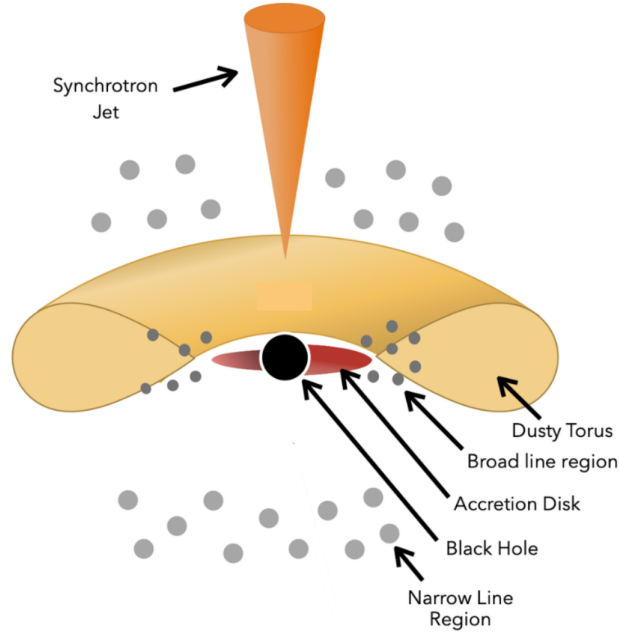


Figure 1.2: Schematic of AGN Components ([Thorne et al. \[2022\]](#))

both sides, called Jets. The magnetic field confines the escaping plasma. Jets may span upto thousands of light years. Because these jets are significant radio emitters, radio telescopes can directly see them.

1.3 Classification of AGN

Depending on their radio emission, AGNs can be divided into radio-quiet and radio-loud categories. In radio-loud objects, the jet and the lobes it inflates make up the majority of their luminosity, at least at radio wavelengths. Jet-related emissions can be disregarded because radio-quiet objects lack a strong jet. In contrast to actual physical differences, AGN terminology is primarily based on historical facts regarding how objects were first discovered or categorised.

1.3.1 Radio-loud AGN

•Radio-loud quasars

Radio-loud quasars are a subclass of AGN that emit strong radio emission. Around 15% of quasars are radio-loud. These radio emissions are produced

by jets of highly energetic particles ejected from the vicinity of a supermassive black hole at the galaxy's centre. The radio-loudness parameter R is defined as the flux density ratio at 5 GHz to that at 4400Å, and is used to distinguish between radio-loud and radio-quiet AGN. AGN with $R > 10$ is classified as radio-loud.

•Blazars (BL Lac objects and Flat spectrum quasars)

Blazars are AGNs with particle jets and radiation aimed directly at Earth, resulting in relativistic amplification of emitted radiation. They are observable at large distances and are distinguished by rapid flux variability across the electromagnetic spectrum, high polarization, and flat radio spectra. Blazars' unique observational properties are due to the relativistic jet's peculiar motion and Doppler boosting of the jet's luminosity and variability amplitude. Blazars are classified as flat spectra radio quasars and BL Lac objects based on the presence/absence of emission lines in the optical spectra.

•Radio Galaxies

Radio galaxies are a type of AGN that are characterized by jets of particles and radiation emitting at radio wavelengths. Unlike blazars, their jets are viewed at large angles, greater than 30 degrees from the line of sight. They exhibit nuclear and extended radio emissions and are typically hosted by massive elliptical galaxies. The radio emission originates from synchrotron radiation produced by high-energy electrons in the jets as they spiral around magnetic field lines. Radio galaxies are essential in studying the evolution of galaxies and the interplay between black holes and their host galaxies.

1.3.2 Radio-quiet AGN

•Seyfert galaxies

Seyfert galaxies are a type of AGN characterized by optical nuclear continuum emission, strong nuclear X-ray emission, and sometimes a weak small-scale radio jet. These emissions are believed to be caused by the accretion of material onto a supermassive black hole at the galaxy's centre. The hosts of Seyfert galaxies are typically spiral galaxies, as opposed to elliptical galaxies, which are the hosts of radio galaxies. Spiral galaxies have more gas and dust, which can fuel the accretion process, leading to the higher levels of activity seen in Seyfert galaxies. The presence of the small-scale radio jet is thought to be related to the orientation of the accretion disk and the black hole's spin axis ([Wikipedia contributors \[2023\]](#)).

•Radio-quiet quasars

Quasars are the luminous counterparts of Seyfert galaxies. Radio quiet quasars are a type of quasar that do not exhibit significant radio emission. Radio quiet quasars are typically characterized by strong optical and ultraviolet emission, but little to no radio emission. AGN with radio-loudness parameter $R < 10$ is classified as radio-quiet. Radio quiet quasars are important in studying the evolution of galaxies and the role of AGN in shaping their properties. They are also used as probes of the intergalactic medium, as their strong ultraviolet emission ionizes gas in their surroundings, leading to absorption features in their spectra ([Drake \[1975\]](#)).

•Low Ionization Nuclear Emission line Regions (LINERs)

Low Ionization Nuclear Emission line Regions (LINERs) AGN regions exhibiting weak, narrow emission lines of ionized gas. The ionization level of the gas is low, meaning that the atoms have lost relatively few electrons. This is in contrast to high-ionization AGN, such as Seyfert galaxies and quasars, which exhibit robust and broad emission lines of highly ionized gas. LINERs are typically found in the centres of galaxies and are thought to be powered by a low-luminosity AGN or other processes, such as shock waves or hot stars. They are essential in studying the feedback between AGN and their host galaxies, as well as the properties of the interstellar medium in the nuclei of galaxies.

1.4 AGN Unification

AGN unification is a model that seeks to explain the different types of AGN's as manifestations of the same underlying physical processes viewed from different angles. The central engine of an AGN is a supermassive black hole surrounded by an accretion disk of hot gas, which powers the emission of radiation across a wide range of wavelengths. Differences in the observed properties of AGN, such as the presence or absence of broad emission lines or radio emission, can be explained by the orientation of the AGN with respect to the observer's line of sight (viewing angle θ , See figure 1.3). AGN unification provides a powerful framework for understanding the nature of AGN and its role in the evolution of galaxies over cosmic time.

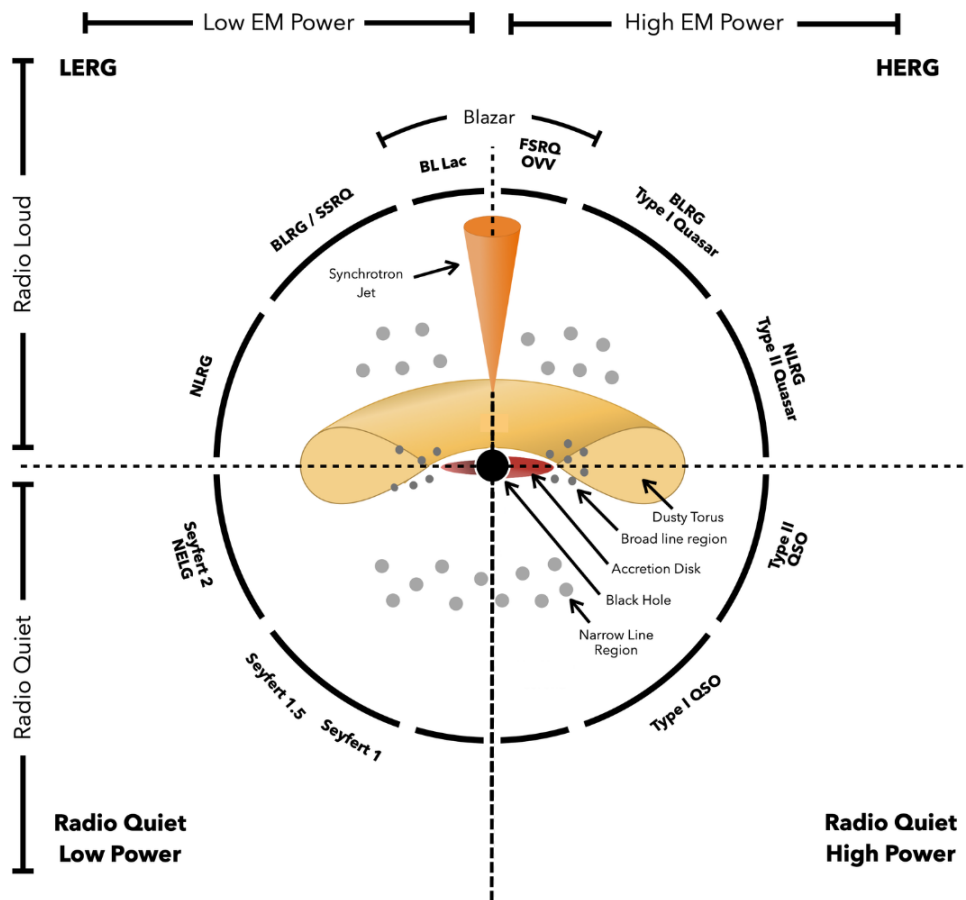


Figure 1.3: Schematic of AGN Unification scheme (Thorne et al. [2022])

Chapter 2

Review of Related Literature

2.1 Quasars

“Quasar”, short for “quasi-stellar objects”, refers to a class of highly luminous and far celestial objects. Some quasars’ centres eject narrow, extremely intense streams of particles called jets, which can travel thousands of light-years across space. Jets are one of the most intriguing characteristics of quasars, among the universe’s most powerful and enigmatic objects. ([Matthews and Sandage \[1963\]](#))

The origin of these jets is thought to be the supermassive black holes that power quasars. When matter falls into the black hole, it forms a disk of hot, glowing gas called an accretion disk. The black hole’s strong gravitational pull causes this gas to spin rapidly, generating enormous heat and pressure that can launch jets of material outward along the black hole’s axis of rotation.

Exactly how this happens is still unclear, but it is thought to result from the interaction of magnetic fields and the swirling gas. As the jets emerge from the accretion disk, they are accelerated to incredibly high speeds and emit intense radiation across the electromagnetic spectrum.

2.2 Classification of Quasars

According to the most current unified models of active galactic nuclei (AGNs), there are two physically separate groups of these objects- radio-loud and radio-quiet. The main observable difference between the two categories is that The radio-loud objects generate large-scale radio lobes and jets, with

the jets' kinetic power representing a sizeable portion of the overall bolometric luminosity. On the other hand, the radio-quiet objects' modest radio ejecta are of little energy significance.

2.3 Relativistic Jets

One of their coolest features of Quasars is the extended jets, which can stretch for thousands of light years and emit beams of radiation that are incredibly powerful. The accretion disk surrounding the supermassive black hole at the centre of the quasar generates these jets. As matter falls towards the black hole, it heats up and emits radiation in the form of X-rays and gamma rays. Some of that energy is converted into kinetic energy, which is then transferred to the jets.

The jets in quasars are often observed in radio wavelengths, where they emit bright, extended radio emission that is associated with the synchrotron radiation from charged particles that spiral along magnetic field lines. The jets themselves are made up of charged particles that are accelerated to near-relativistic speeds (See figure 2.1).

What's particularly interesting about quasar jets is their complex structure. They often exhibit knots and filaments, which are thought to be caused by shocks and instabilities in the jets. It is possible to deduce information about the surroundings of a black hole, such as the intensity and direction of the magnetic field, from the structure of quasar jets.

Studying the extended jets in quasars is really important for understanding the evolution of galaxies and the role of black holes in shaping their properties. Jets can transport energy and matter across large distances, and may play a role in regulating the growth of galaxies and the formation of stars. They're also a great way to study the physics of particle acceleration and magnetic fields in extreme environments.

Relativistic jets can significantly impact their environment, as they can transport energy and matter over vast distances. They can also produce intense radiation across the electromagnetic spectrum, from radio waves to gamma rays.

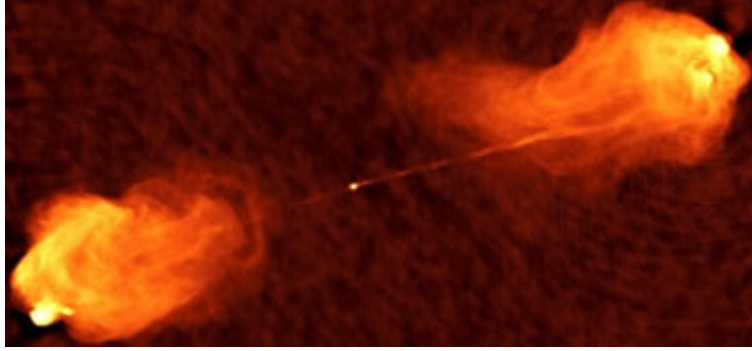


Figure 2.1: The Radio Galaxy Cygnus A as seen at 1.4 GHz. ([NRAO/AUI](#))

2.4 Motivation of the Work

The energy produced by the supermassive black hole (SMBH) at the centre of active galactic nuclei is transported over vast distances (>100 kpc) by jets. In the early universe, the effects of jets on the surrounding environment play a role in the development and evolution of structures. When seen at modest angles to the line of sight, radio-loud quasars' radiation from the innermost jets (parsec scales or smaller) can be Doppler boosted.

Relativistic Jets can therefore give useful observational information of the state of SMBH activity. Over their lifetime, large-scale X-ray jets record the history of SMBH activity at distances of up to hundreds of kiloparsecs. The Chandra X-ray Observatory, due to its excellent imaging capabilities, has successfully resolved jets at X-ray energy band (0.5 - 7 keV).

Even while the number of these X-ray jets has significantly increased since Chandra's launch in 1999, it is still relatively minor compared to the total number of recognised quasars. Only a small number of the about 100 large-size X-ray jets discovered so far have high-quality X-ray morphology data. Detecting X-ray jets is intrinsically difficult because of the low number of X-ray photon counts obtained from jets compared to their respective quasar cores. Therefore identifying and characterizing extended X-ray jets is of at most importance to understand their morphology, particle acceleration process and radiation mechanisms responsible for the observation of these enigmatic structures. This is the motivation of the project

To achieve this objective, we have used the publicly available tool, multi-scale Bayesian method known as Low count Image Reconstruction and Analysis (LIRA). The algorithm models the residual as a multi-scale component

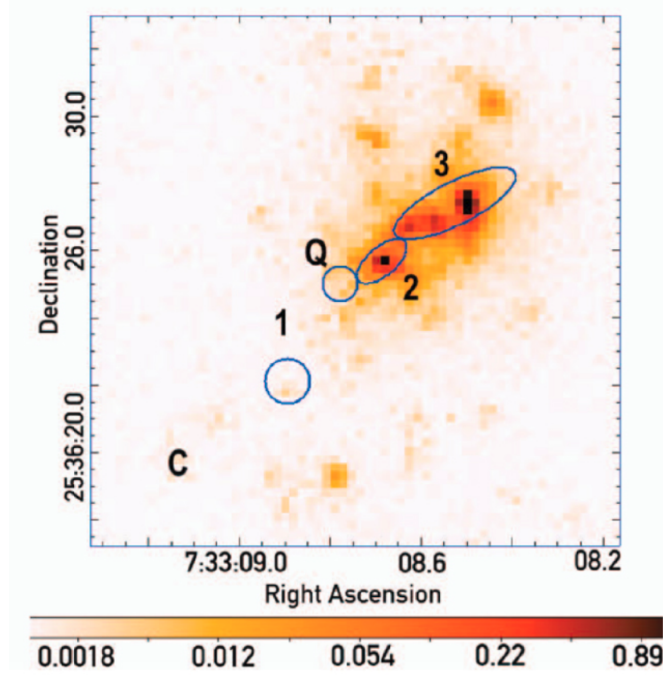


Figure 2.2: 0.5 - 7 keV image of the Quasar 073+257 taken with the Chandra X-ray observatory. Different selected regions are highlighted and numbered. Figure adopted from [McKeough et al. \[2016\]](#).

and generates a series of images that capture the emission that may be present more than the baseline model. We can then compute a p-value by generating a series of Monte Carlo simulations of images under the baseline model and fitting each of these simulated images using LIRA. The details are described in the later chapters.

Chapter 3

Data Analysis and Methodology

3.1 *Chandra* X-Ray Observatory

The *Chandra* X-ray Observatory (CXO) is made for high-resolution (0.492 arcsec) X-ray imaging and spectroscopy. It was launched on July 23, 1999, to detect X-ray emissions from very hot regions. Four extremely delicate mirrors that are nested inside of one another are carried by *Chandra*. Between 0.1 and 10 keV, it offers good sensitivity.

Chandra X-Ray Observatory and its instruments are shown in figure 3.1. X-ray imagers include the Advanced CCD Imaging Spectrometer (ACIS). Each X-ray photon striking the camera is identified, and information about its position, energy, and arrival time is recorded. The ACIS includes two CCD arrays, one (ACIS-I) designed for large fields (16x16 arc minutes) imaging and the other (ACIS-S) designed as a readout for the HETG transmission grating. The greatest energy resolution of the ACIS system is provided by one chip of the ACIS-S (S3), which may also be utilised for on-axis (8x8 arc minutes) imaging. Enables timing investigations, moderate resolution spectroscopy, and imaging with a more excellent resolution (1 arcsec). The back-illuminated S3 chip provides the best spectral resolution without the need for grating.

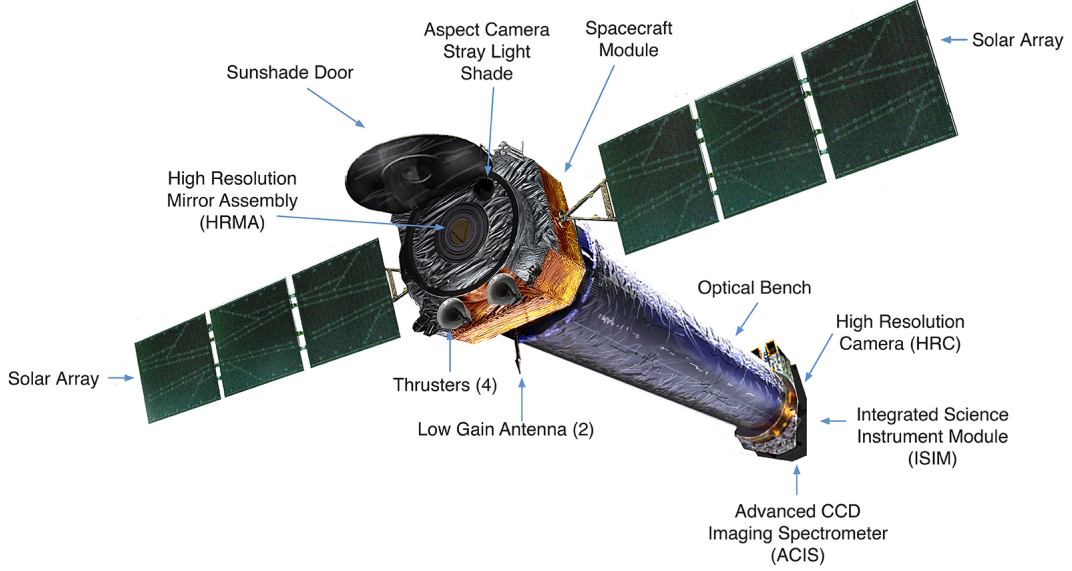


Figure 3.1: *Chandra* X-Ray Observatory Instruments. (Figure adopted from NASA/CXC/SAO)

3.2 *Chandra* Data

We used the conventional techniques described in *Chandra* Interactive Analysis of Observations (CIAO) threads to reprocess the data of target of interest after retrieving it from the *Chandra* repository¹. We used calibration data from CALDB v4.10.2 and CIAO v4.15 (Fruscione et al. [2006]). We examined the light curves for any background flares and if found omitted those time periods. Only events with energies between 0.5-7 keV were taken into account, and counts from pixels with exposure times of less than 2% were disregarded in the final binned picture. We binned all of the event files using the ACIS-S instrument’s half-pixel boundaries (bin size: 0.492 arcsec) uniformity. To meet the criteria of the LIRA input, we adjusted the picture size to even powers of two (64×64 pixels for smaller photos and 128×128 pixels for bigger ones). We selected the source PKS 065-08 (ObsID: 12056) for testing and calibrating our pipeline.

¹<http://cxc.harvard.edu/ciao/guides/index.html>

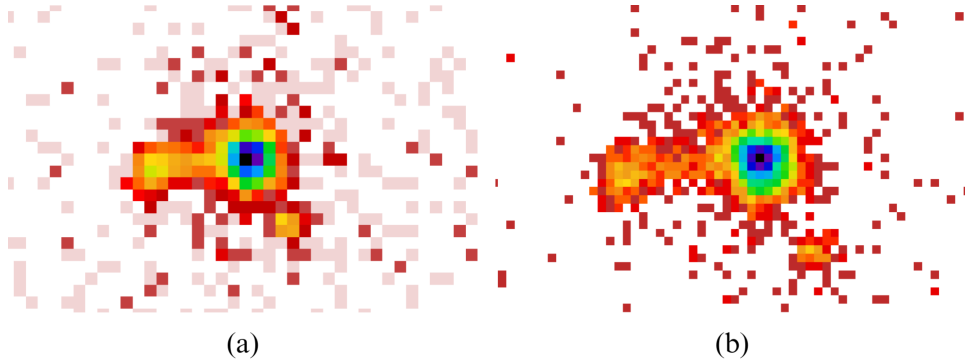


Figure 3.2: (a) Raw 0.5-7 keV image of quasar PKS 065-08, (b) exposure corrected and binned to 0.492 arcsec image of quasar PKS 065-08

3.3 *Chandra* Interactive Analysis of Observations (CIAO)

In order to analyse data from the *Chandra* X-ray Telescope, the *Chandra* X-Ray Center (CXC) created a software called CIAO. CIAO has a terminal-based command line interface. All the tools required for fetching data and data analysis are provided in that package.

3.4 Downloading and Calibrating Data

The *Chandra* Data Archive contains all the data obtained with the *Chandra* telescope. The `download_chandra_obsid` command provides a simple command-line interface to the *Chandra* Data Archive. It requires only the ObsID that you wish to download. The CXC encourages users to reprocess their data to ensure that they have the latest calibrations consistent with the current CALDB. For that, `chandra_repro` command is used.

The image obtained after reprocessing the data of observation id 12056 is shown in Figure 3.2 (a). Chandra Search and Retrieval (ChaSeR) interface is the web interface to the Chandra Data Archive. It allows users to browse the observation catalog with a variety of search criteria, to display preview images, and to download the data tarfiles. ChaSeR allows users to download the standard primary and secondary packages.

3.5 Creating exposure Corrected Image

A co-added, exposure-corrected picture is produced by the `flux_obs` script from a stack of event files after each observation's exposure maps have been created and divided. Result is shown in Figure 3.2 (b). The image can also be generated in different energy bands. The event files are presumed to have the same tangent point or have previously been re-projected. Along with creating an exposure-corrected image, `flux_obs` generates the exposure map for the observation, which is required to run LIRA.

3.6 Generating PSF

The response of a focused optical imaging system to a point source or point object is described by the point spread function (PSF). The PSF, also known as the impulse response or impulse response function (IRF) of a focused optical imaging system, is referred to in a more general sense as the system's impulse response. A measurement of the effectiveness of an imaging system is the amount of spreading (blurring) in the picture of a point object.

Point Response Function describes the form of the picture generated by a delta function (point) source on the detector (PRF). *Chandra* can study X-ray sources with excellent angular and spectral resolution because of its focusing X-ray optics. Understanding the PSF's properties is essential to this research. The HRMA PSF, the aspect, the constrained pixel size of the detector, and the detector effects all contribute to the blurring of the *Chandra* PSF. The first step in getting a decent model of the *Chandra* PSF for a particular observation is to simulate the HRMA PSF using Chandra Ray Tracer (ChaRT).

The spectral energy distribution of the source and its placement within the telescope's field of view (FOV) significantly impact the size and form of the HRMA PSFs. The Wolter Type I design ensures optimal picture quality in a narrow region centred on the optical axis. Specifically, the mirrors were made to concentrate more than 85% of the energy at 0.277 keV inside a 1 arcsec diameter and generate pictures with greater than one arc-second resolution.

The ChaRT simulates the best possible PSF for a point source at any off-axis angle and for any energy or spectrum. Position and energy both affect the *Chandra* PSF. ChaRT users can specify the spectral form as either

a single monochromatic energy or by uploading the spectrum as a file.

To run ChaRT, we need to follow the below mentioned steps:

3.6.1 Generating Spectrum File:

Users can upload a file to ChaRT that details the source's spectrum. The file's format is any format that the CXC datamodel supports. (FITS and various ASCII formats). The document has to be a table with just three columns. The lower and higher energy bounds, expressed in keV, must be in the first two columns, with values that must range from 0.2 to 10.0 keV. The photon flux is measured in the third column in units of $photon/cm^2/sec$, and its values must be greater than 0. The column names and any other meta-data (such as keywords) are not taken into account.

Using the outcomes of a linear spectral fit is one way to generate the input spectrum. The pulse height spectrum from the observation is then extracted. To extract the energy spectrum from the events file, **specextract** command is used in the CIAO interface alongwith specifying the centre coordinates of the source. To fit the spectrum with an absorbed powerlaw spectrum, we use **sherpa** package.

Sherpa is the CIAO modeling and fitting application. It enables the user to construct complex models from simple definitions and fit those models to data, using a variety of statistics and optimization methods. To fit the spectrum, we use **xsphabs.abs1*powlaw1d.p1** where **xsphabs** is a multiplicative model component representing photoelectric absorption and **i. powlaw1d** is a one-dimensional power-law function. The fitted spectrum for PKS 065-08 is shown in figure 3.3. Later we implement **save_chart_spectrum()** command from the **sherpa.contrib.chart** module may be used to create the output spectrum file (.dat format) which is to be uploaded on ChaRT website.

3.6.2 Retrieving ChaRT Rays

The SAOsac raytrace code's web interface, ChaRT, was created by the CXC for calibration reasons. The *Chandra* optics process a raytrace that matches the user inputs to create a collection of rays. The user receives an email when the raytrace data is ready for download.

The tar file generated by ChaRT contains all the requested ray files (one for each iteration). The columns listed in the output rayfile are:

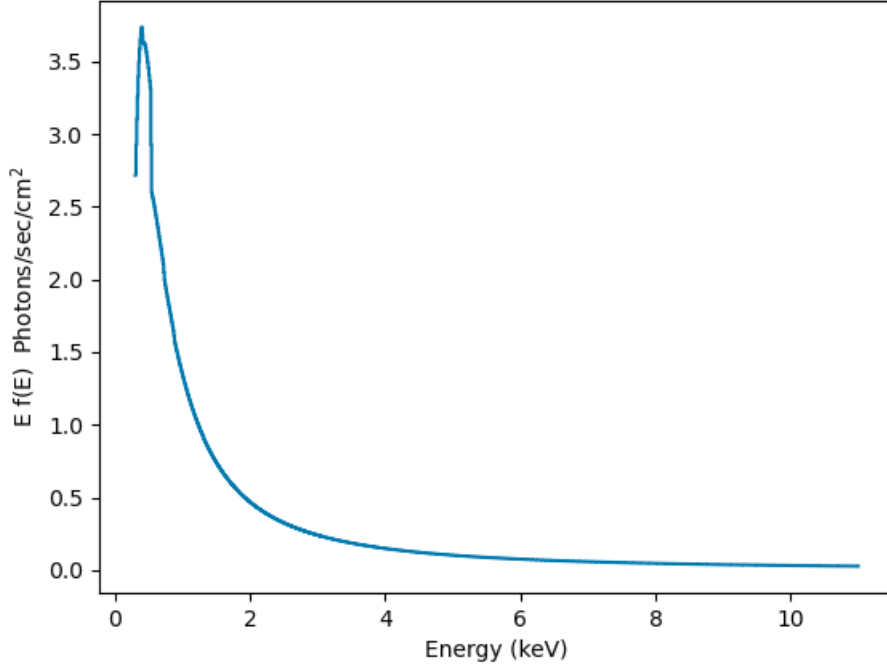


Figure 3.3: Energy Spectrum of PKS 065-08 generated by `specextract` command.

1. `rt_cosx`, `rt_coxy`, `rt_cosz`: cosine of the ray direction.
2. `rt_x`, `rt_y`, `rt_z`: ray position in telescope coordinates (in millimeters)
3. `rt_time`: The time of the ray. Since this simulation used an aspect solution (retrieved by `OBS_ID`), the time range in the ray file match the times in the aspect solution file.
4. `rt_wght`: fractional probability that this ray will reach the focal plane.

3.6.3 Using MARX to Create an Event file from ChaRT Rays

By using MARX, the user can include all modifications to the photon distribution originating from the HRMA brought on by the detector response.

The MIT/CXC/HETG collaboration developed and maintained the `marx` software package, which enables users to emulate the *Chandra* X-ray Observatory's on-orbit performance. With the ability to produce common FITS

event files and photos as an output, *marx* offers a thorough ray-trace simulation of how *Chandra* reacts to various astrophysical sources.

For *Chandra*'s High-Resolution Mirror Assembly (HRMA), the HETG and LETG gratings and all of the focal plane detectors, *marx* include comprehensive models. Along with modelling detector response, MARX also utilises ray weights to account for mirror effects, or the different shells' efficiencies at various angles and energies.

In order to generate the psf, we followed the procedure mentioned below:

1. Activate *marx* in the *ciao* environment.
2. Getting Source Coordinates: Before running the simulation, it is necessary to determine the nominal celestial position of the telescope optical axis. These values are stored in the header of the level=2 events file. It is obtained by using `dmlist (filename) header | grep NOM`.
3. Additionally, the celestial coordinates of the source for the PSF are required. Their values are stored in the ChaRT header file. They can be extracted by running `dmlist (filename) header | egrep "SRC_(RA|DEC)"`.
4. Generating psf using `simulate_psf` command: The `simulate_psf` script automates the steps needed to run the ChaRT generated ray files, run them through *marx*, and produce an image of the PSF (Figure 3.4 (a)).

In order to fit our data, we used the Levenberg-Marquardt optimisation process and the χ^2 -statistic with Gehrels variance function. We utilised MARX v5.5.2 (Davis et al. [2012]) as the backend to simulate the PSF of the core and submitted the fitted model to the `simulate_psf` module in CIAO. To get the final PSF, we produced 100 iterations across each source. To guarantee that we sampled the same region of the PSF as the core, we also matched the simulated PSF's pixel boundaries with its corresponding input picture. When simulating a PSF using MARX, the aspect is reconstructed by convolution of the PSF with a Gaussian model. The default value for the variance in this Gaussian model (the `blurr` option in `simulate_psf`) is 0".07.

Historically, this number generated a narrower PSF at lower radii and wider PSF wings than a simple ACIS-S observation (Primini et al. [2011]), and this discrepancy has never been addressed. According to a preliminary examination of specific observations made by the MARX team, a value of

$\approx 0''.25$ provided a better matching PSF at smaller radii. A more significant value of $\approx 0''.28$ provided better matching PSF wings for the ACIS-S sensor.² No analytical techniques exist to calculate the precise value, which depends on the source spectrum. As a result, we used simulations of PSFs with `blur` values between 0.0 and 0.35 and a step size of 0.01 to determine the `blur` that best matched the observation at both smaller and greater radii.

In order to create a baseline model for each source, we used the methodology described in [McKeough et al. \[2016\]](#). We used SHERPA to fit a 2D Gaussian model with a fixed backdrop and the core’s simulated PSF to the sub-pixel picture. After that, we used SHERPA’s fake function to replicate 50 photos of the fitted model. The baseline model was also impacted by changing the blur value. The Gaussian model with the preset blur has a complete width at a half-maximum greater than one pixel. It is also consistent with the hypothesis that the core is a point source that the best-matching blur produced a delta-like function.

3.7 LIRA: Low-counts Image Reconstruction and Analysis

Detecting the X-ray beam is particularly challenging because it is a faint structure near the quasar’s much more powerful core. The Bayesian multistage LIRA³ method is well suited to this challenge. An efficient feature detection method is described in [Stein et al. \[2015\]](#) as a complement to the multilevel shaper. Section 2 of Document I details the statistical models used by LIRA, which we briefly summarize here. We consider square images of $n=2^d \times 2^d$ pixels, where d is an integer. The fundamental idea behind LIRA is to model an image as a combination of two separate “components,” each of which contributes to a single pixel. The initial model component is the user-specified “baseline component”, which incorporates any elements we are aware of or presume to be present (such as the point-source core and a constant background). The “added component” is defined individually (per-pixel basis), although it is implied based on comparing the real data to the baseline model.

LIRA uses a multi-scale representation of an observation, first employed to calculate the uncertainties in X-ray image deconvolution. (known as

²<https://cxc.cfa.harvard.edu/ciao/why/aspectblur.html>

³<https://github.com/astrostat/LIRA>

EMC2, Esch et al. [2004]). LIRA derives the additional component by fitting the whole model to the observation using this representation, which permits flexible departures from the baseline component. The posterior of the image parameters, or the pixel values in both components, is computed specifically given the observation. The observed picture may be recreated by convolving it with the PSF. The superposition of the two model components (baseline and added) gives the underlying brightness distribution in each pixel.

The test makes use of the tail probability of the posterior of ξ (Equation (11) in Stein et al. [2015]) for the observed picture, where ξ is the percentage of the total emission (baseline+added) from the added component inside a designated ROI. The upper tail probability (γ) of a combined posterior ξ , produced from several simulations of the baseline component, is fixed to a fair value to determine the tail's position. This test shows if the baseline component's real observation and simulated photos have different distributions. Therefore, a sizable difference between the two distributions would suggest the presence of an important extra component (such as emission from the jet) in the observation.

3.8 Quantifying Evidence for Extended Jet Emission Using LIRA

LIRA utilises a composite Gaussian plus constant baseline model, a ray-traced *Chandra* PSF, and a binned *Chandra* image for the quasar core and background. A series of simulated images of the residual multi-scale component, including any non-Poisson deviations from the baseline model, are returned by the MCMC sampler in LIRA. In the situations examined, these simulations suggest the presence of a jet originating from the X-ray quasar. The fitted image of the multi-scale component comprises only random fluctuations if the *Chandra* image agrees with the base model (quasar core + background). Any X-ray emission that is not covered by the baseline component, on the other hand, manifests as a systematic departure from this noise. Significant deviations can be used as *Chandra*'s image as evidence for structures other than the baseline component.

The formal statistical hypothesis test for the presence of structure (such as a quasar jet) in the new multi-scale component is described in Section 3 of Stein et al. [2015], along with a method for computing an upper bound on the test's p-value. When there is no additional structure in the X-ray

image beyond the baseline model, Monte Carlo evaluation of the behaviour of the fitted multi-scale component—which characterises the departure from the baseline image is required. (i.e., when there is no jet). In terms of numbers, this entails quickly computing an upper bound on the p-value using a test statistic. We briefly describe this approach here; [Stein et al. \[2015\]](#) has additional details.

Using Sherpa’s fake function, we first generate 50 duplicate pictures under a baseline-only model for each observed image. The baseline model is based on the best-fit values obtained by fitting a 2D model, `psf*gauss2d+const2d`, to the observed X-ray image. It consists of a 2D Gaussian for the quasar core on top of a constant background. We run LIRA⁴ on each quasar and discard the first 1000 images from *Chandra* and each of its 50 duplicate baseline-only simulated images.

When the deviation from the baseline is fitted to simulated images, the image contains random fluctuations; however, when it is fitted to *Chandra* images, it also includes estimations of any additional structure. If the ROI signal is higher than expected from random fluctuations using the baseline-only model, a jet is said to have been spotted. So, we must compare the 50 matching fitted deviations from the baseline-only simulations with the fitted deviations from the *Chandra* observation’s baseline. A unique test statistic described in [McKeough et al. \[2016\]](#) is implemented to do this quantitatively.

3.9 Using Python and *pylira*

LIRA is an R language-based simulation program. It requires a binned image of the events file (figure 3.2 (a)), the spectrum of the core (figure 3.3), the power-law model, PSF (figure 3.4 (a)) and a simulated baseline image (figure 3.4 (d)) and exposure of the observation (figure 3.4 (c)) as inputs to run the MCMC simulation and reconstruct the image along with producing the p-value. We have been developing a single Python programming language-based pipeline to execute the whole process from the beginning by binning the image till producing the Posterior Distribution plot and the reconstructed image. We can integrate CIAO tools into Python code by importing the `ciao.contrib.runttools` library provided along with the CIAO package. It is helpful to use Python as it allows executing the parameters per the users’ needs and obtaining better results than before.

⁴We only employ LIRA iterations generated after the MCMC sampler has been burned in once. For each run, we always get 2000 iterations.

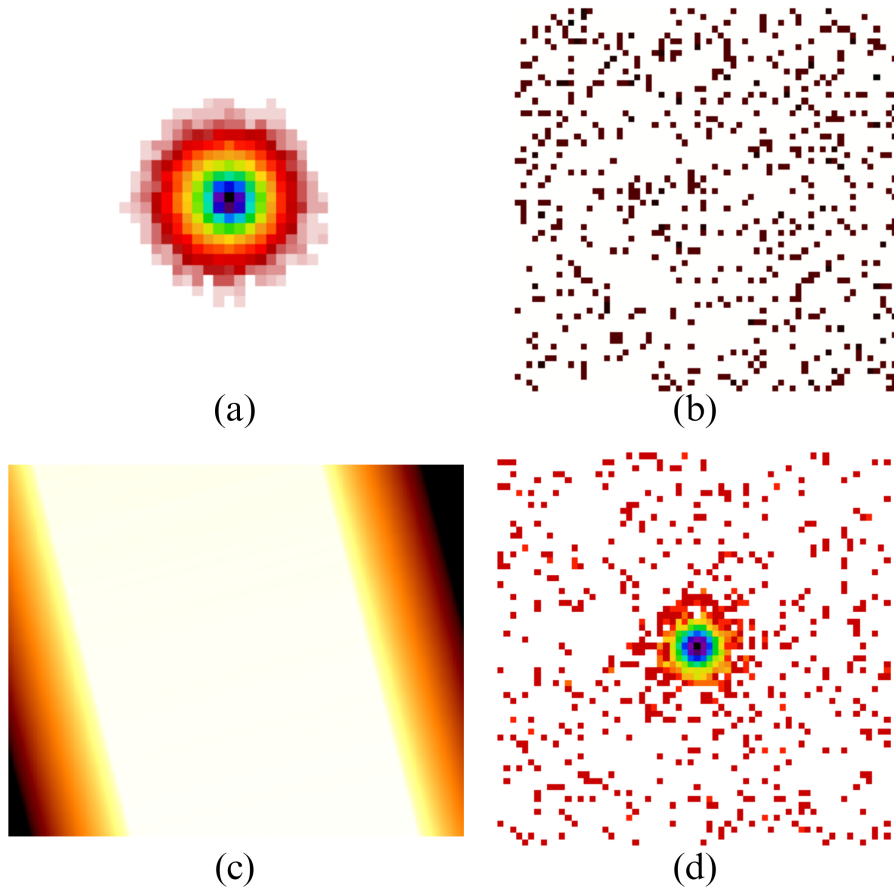


Figure 3.4: (a) PSF of PKS 065-08 generated by `marx`, (b) background image of PKS 065-08, (c) Exposure image of PKS 065-08, (d) simulated baseline model for PKS 065-08 using `fake` function.

We developed multiple libraries to carry out different functions such as estimating the blur parameter, computing offset, generating mask, rebinning image, generating psf, etc for performing the steps mentioned earlier. We later imported these libraries into a single code for better execution. The LIRA simulation has been executed using a Python package called *pylira*⁵. It requires R language installation for its execution. Pylira is basically an integration tool between R and Python to simulate MCMC in Python.

⁵<https://pylira.readthedocs.io/>

Chapter 4

Results

The project’s primary goal is to find traces of extended emissions outside of the PSF of a Radio-loud Quasar. It is achieved using MCMC simulations offered by LIRA and proving the existence of an extended emission using statistical analysis.

To test our pipeline and the LIRA processing, we first run the example dataset given on the pylira website to match their results with our pipeline—the results of their posterior mean distribution as shown in the figure 4.1. We got the exact same results as prescribed in the documentation of LIRA.

For our source PKS 0605-08, We first simulated LIRA for 5000 iterations, discarded the first 200 iterations for the sampling process to converge on the 50 simulated images and took a mean of the results of these processes. Then we ran the LIRA for the original observation and recorded the results. The comparison of the obtained p-values shown in the figure 4.2. We ran LIRA for two regions, i.e. for the core region (A) and the jet region (B). As per the hypothesis, the posterior mean of simulated and observed simulations should overlap, as seen in the figure 4.2 (c), whereas, for the jet region, no emission for the B region observed in the simulated images; thus, they are expected to be different, as seen in the figure 4.2 (d). Thus, we conclude that we detect an extended emission at the B region other than the core and the psf.

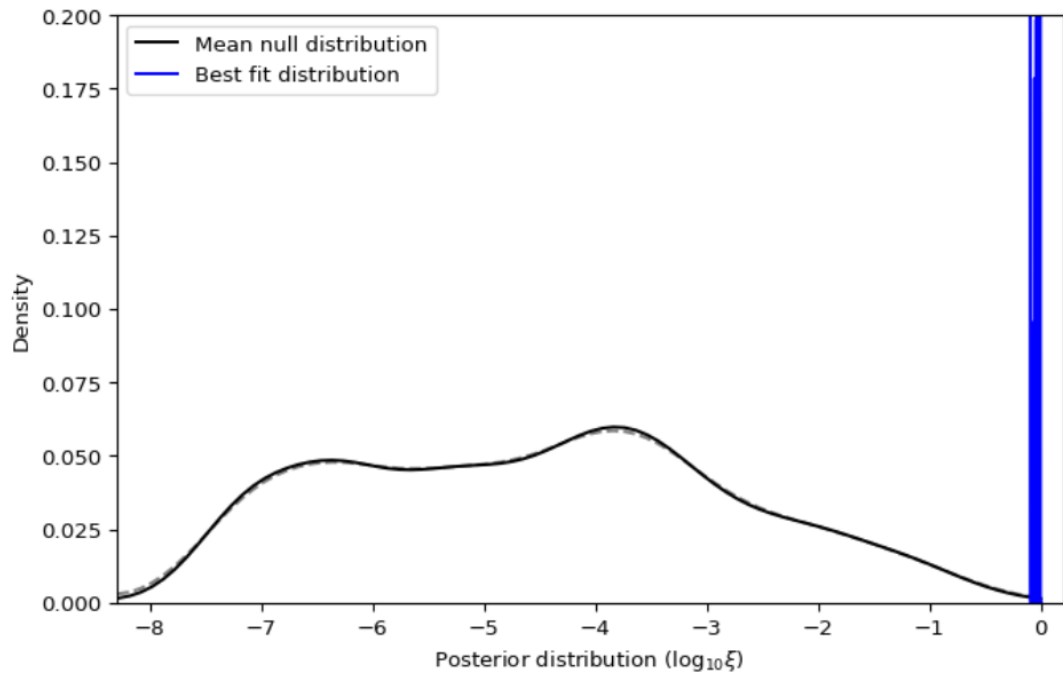


Figure 4.1: Test plot obtained by running the pipeline for the demo dataset. The black line is the posterior distribution of the simulated baseline model, and the blue line is for the demo dataset used in the pylira documentation. Both distributions do not overlap each other, indicating the presence of an extended emission at the selected region.

PKS 065-08

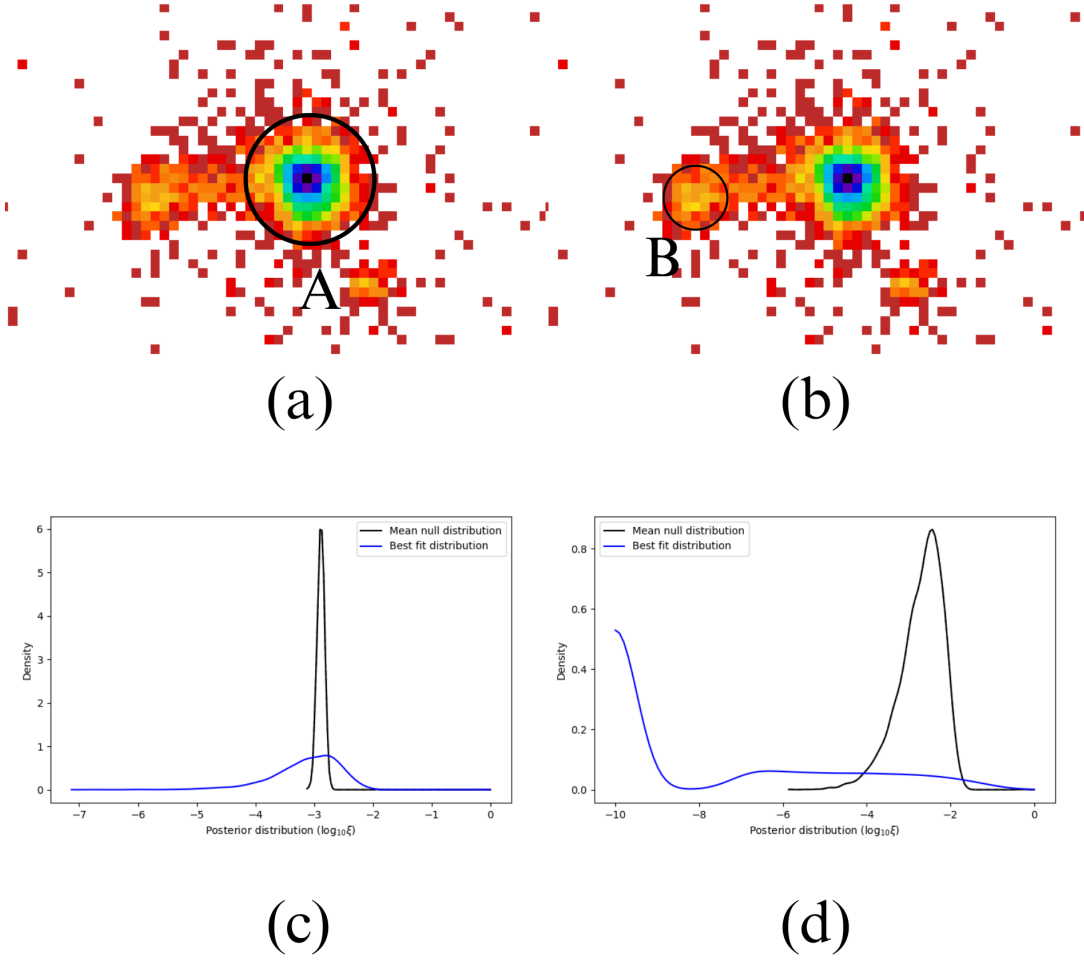


Figure 4.2: Images, regions of interest (ROIs), and results for quasar PKS 0605-08. (a,b) The observed Chandra ACIS-S image with colors indicating photon counts with fitted regions of Interests A and B. A is the center core region and B is the jet region. (c) The posterior distributions of ξ in each ROI for the data (blue solid curve), the average of 50 simulated replicate images under the null model, which includes the quasar and a background but not a jet (black solid curves).

Chapter 5

Conclusion

We developed a pipeline to statistically test the presence of extended emission from a radio-loud Quasar. It is difficult to identify the extended emission visually in low-count data, so we require a statistical simulation that compares the simulated results with the observed data and tests for the extended emission. Here, we developed the pipeline, successfully testing the hypothesis. It can independently work for any low-count X-ray data of any telescope. We tested it for the example data set and obtained similar results. Also, we implemented it on the sources analysed in the paper [Solipuram et al. \[2021\]](#), whose data was obtained from the Chandra X-ray telescope and obtained similar results to prove that our pipeline is successfully working.

Further in this project, we can run LIRA to reconstruct the image to a better resolution. We can get an even better view of the extended emission, which is very beneficial for the morphological study of the Quasar.

We tested our pipeline for a known result; we can extend it on the data if low-counts X-ray data of radio-loud Quasars and test for the presence of extended emission. If we detect it, we can observe it in radio bandwidth and other wavelengths and carry out a multi-wavelength morphological analysis of the Quasar. This way, a detailed catalogue of various Quasars can be prepared with good-quality morphological data to carry out the science.

Bibliography

- Jessica Thorne, Aaron Robotham, Luke Davies, and Sabine Bellstedt. Agn unification diagram, March 2022. URL <https://doi.org/10.5281/zenodo.6381013>. Was originally created to be included in the introduction of Thorne J. E., et al., 2022, MNRAS, 509, 4940.
- Wikipedia contributors. Seyfert galaxy — Wikipedia, the free encyclopedia. https://en.wikipedia.org/w/index.php?title=Seyfert_galaxy&oldid=1146778964, 2023. [Online; accessed 2-May-2023].
- F. D. Drake. Radio astronomy: j̃galactic and extra-galactic radio astronomỹĩ. gerrit l. verschuur, kenneth i. kellerman, and virginia van brunt, eds. springer-verlag, new york, 1974. xii, 402 pp., illus. \$37.80. *Science*, 188 (4187):444–444, 1975. doi: 10.1126/science.188.4187.444.a. URL <https://www.science.org/doi/abs/10.1126/science.188.4187.444.a>.
- Thomas A. Matthews and Allan R. Sandage. Optical Identification of 3C 48, 3C 196, and 3C 286 with Stellar Objects. *ApJ*, 138:30, July 1963. doi: 10.1086/147615.
- NRAO/AUI. Relativistic jet. URL <https://astronomy.swin.edu.au/cosmos/g/Galactic+Jets>. A radio image of the galaxy Cygnus A clearly shows the jet and radio lobes. The ‘hot spots’ that mark the shock fronts between the jet and the interstellar medium are clearly evident.
- Kathryn McKeough, Aneta Siemiginowska, C. C. Cheung, Łukasz Stawarz, Vinay L. Kashyap, Nathan Stein, Vasileios Stampoulis, David A. van Dyk, J. F. C. Wardle, N. P. Lee, D. E. Harris, D. A. Schwartz, Davide Donato, Laura Maraschi, and Fabrizio Tavecchio. DETECTING RELATIVISTIC x-RAY JETS IN HIGH-REDSHIFT QUASARS. *The Astrophysical Journal*, 833(1):123, dec 2016. doi: 10.3847/1538-4357/833/1/123. URL <https://doi.org/10.3847%2F1538-4357%2F833%2F1%2F123>.
- Antonella Fruscione, Jonathan C. McDowell, Glenn E. Allen, Nancy S. Brickhouse, Douglas J. Burke, John E. Davis, Nick Durham, Martin Elvis,

- Elizabeth C. Galle, Daniel E. Harris, David P. Huenemoerder, John C. Houck, Bish Ishibashi, Margarita Karovska, Fabrizio Nicastro, Michael S. Noble, Michael A. Nowak, Frank A. Primini, Aneta Siemiginowska, Randall K. Smith, and Michael Wise. CIAO: Chandra’s data analysis system. In David R. Silva and Rodger E. Doxsey, editors, *Observatory Operations: Strategies, Processes, and Systems*, volume 6270 of *Society of Photo-Optical Instrumentation Engineers (SPIE) Conference Series*, page 62701V, June 2006. doi: 10.1117/12.671760.
- John E. Davis, Marshall W. Bautz, Daniel Dewey, Ralf K. Heilmann, John C. Houck, David P. Huenemoerder, Herman L. Marshall, Michael A. Nowak, Mark L. Schattenburg, Norbert S. Schulz, and Randall K. Smith. Raytracing with MARX: x-ray observatory design, calibration, and support. In Tadayuki Takahashi, Stephen S. Murray, and Jan-Willem A. den Herder, editors, *Space Telescopes and Instrumentation 2012: Ultraviolet to Gamma Ray*, volume 8443 of *Society of Photo-Optical Instrumentation Engineers (SPIE) Conference Series*, page 84431A, September 2012. doi: 10.1117/12.926937.
- Francis A. Primini, John C. Houck, John E. Davis, Michael A. Nowak, Ian N. Evans, Kenny J. Glotfelty, Craig S. Anderson, Nina R. Bonaventura, Judy C. Chen, Stephen M. Doe, Janet D. Evans, Giuseppina Fabiano, Elizabeth C. Galle, Danny G. Gibbs, John D. Grier, Roger M. Hain, Diane M. Hall, Peter N. Harbo, Xiangqun Helen He, Margarita Karovska, Vinay L. Kashyap, Jennifer Lauer, Michael L. McCollough, Jonathan C. McDowell, Joseph B. Miller, Arik W. Mitschang, Douglas L. Morgan, Amy E. Mossman, Joy S. Nichols, David A. Plummer, Brian L. Refsdal, Arnold H. Rots, Aneta Siemiginowska, Beth A. Sundheim, Michael S. Tibbetts, David W. Van Stone, Sherry L. Winkelman, and Panagoula Zografou. Statistical Characterization of the Chandra Source Catalog. *ApJS*, 194(2):37, June 2011. doi: 10.1088/0067-0049/194/2/37.
- Nathan M. Stein, David A. van Dyk, Vinay L. Kashyap, and Aneta Siemiginowska. Detecting Unspecified Structure in Low-count Images. *ApJ*, 813(1):66, November 2015. doi: 10.1088/0004-637X/813/1/66.
- David N. Esch, Alanna Connors, Margarita Karovska, and David A. van Dyk. An Image Restoration Technique with Error Estimates. *ApJ*, 610(2):1213–1227, August 2004. doi: 10.1086/421761.
- K. Solipuram, M. Georganopoulos, and E. Meyer. X-Ray-to-Radio Offset Inference from Low-Count X-Ray Jets. In *American Astronomical Society*

Meeting Abstracts, volume 53 of *American Astronomical Society Meeting Abstracts*, page 209.05, January 2021.